Physics Letters B 760 (2016) 800–806

Contents lists available at ScienceDirect

Physics Letters B

www.elsevier.com/locate/physletb

Possible origin of transition from symmetric to asymmetric fission

H. Pașca [a,b], A.V. Andreev [b], G.G. Adamian [b,*], N.V. Antonenko [b,c]

[a] "Babeș-Bolyai" University, 400084 Cluj-Napoca, Romania
[b] Joint Institute for Nuclear Research, 141980 Dubna, Russia
[c] Mathematical Physics Department, Tomsk Polythechnic University, 634050 Tomsk, Russia

ARTICLE INFO

Article history:
Received 26 June 2016
Received in revised form 19 July 2016
Accepted 28 July 2016
Available online 3 August 2016
Editor: V. Metag

Keywords:
Binary fission
Charge distributions
Scission-point model
Dinuclear system model

ABSTRACT

The charged distributions of fragments produced in the electromagnetic-induced fission of the even–even isotopes of Rn, Ra, Th, and U are described within an improved scission-point model and compared with the available experimental data. The three-equal-peaked charge distributions are predicted for several fissioning nuclei with neutron number $N = 136$. The possible explanation of the transition from a symmetric fission mode to an asymmetric one around $N \sim 136$ is presented. The excitation energy dependencies of the asymmetric and symmetric fission modes are anticipated.

1. Introduction

The measured charge (mass) distributions resulting from the fission of pre-actinides are usually symmetric, while the measured charge distributions in fission of nuclei U–Cf are known to be asymmetric [1–3]. The experimental [2] charge distributions in the electro-magnetic induced fission ($E_\gamma = 11$ MeV) of even–even isotopes ^{218,220,222}Th are clearly symmetric, with one relatively narrow peak around $Z/2 = 45$. For ^{224}Th, the distribution starts showing the formation of two asymmetric peaks, while for the ^{224}Th the yields around Kr–Sr and their complementary fragments are equal to those around Pd–Ru. As the mass number of the Th increases to $A = 228$, the symmetric peak recedes and the asymmetric mode becomes dominant. The yields of symmetric fragments do not go abruptly to zero; the central maximum still exists and the yields are a few times smaller than those of asymmetric ones. The measured charge distributions of fissioning $^{224-228}$Pa nuclei show a similar pattern as in the case of Th isotopes. The nuclei ^{226}Th and ^{226}Pa with neutron numbers $N = 136$ and 135, respectively, have charge distributions with three equal peaks. Thus, with increasing neutron number the transition from one-peaked to two-peaked charge distribution occurs through transient three-peaked shape in which the symmetric and asymmetric components of the distribution have almost equal weights. An immediate question arises: are there isotopes of other nuclei for which the charge yields show a similar transition? Does this transition happen at the same neutron number? Our predictions, shown here, point out that such transitions occur in nuclei ^{A}Rn, ^{A}Ra, and ^{A}U at $N = A - Z \approx 136$. One of other motivating factors of our work is the general opinion that at high excitation energies the charge/mass distributions should all be symmetric, while the experiment [4] showed that for ^{238U}(n,f) the asymmetric shape is conserved even at 60 MeV neutron energy. Note that the transition from symmetric to asymmetric fission are studied in Refs. [5,6]. However, this transition is not completely explained yet.

In the present paper, the origin of the evolution of the charge distribution with increasing neutron number is studied within the scission-point model. The potential energy near the scission point was shown with the dynamical model [6] to govern the final mass (charge) distribution. The reliability of this conclusion is supported by a good description of various experimental data with the scission-point models [7–15]. Our model differs from the model of Ref. [7] by better definition of the scission configuration and the excitation energy, and from the model of Ref. [8] by better definition of the scission configuration and by the inclusion of the deformations of the fission fragments into account. The distance between the tips of the fission fragments at scission and the excitation energy are not the parameters of our model but are defined from the nucleus–nucleus potential. The multidimensional aspect of the driving potential is paramount for the subject tackled in this paper.

* Corresponding author.
E-mail address: adamian@theor.jinr.ru (G.G. Adamian).

http://dx.doi.org/10.1016/j.physletb.2016.07.074

The paper is organized as follows: in Sect. 2 the model employed is described; in Sect. 3 the calculated results are presented; and in Sect. 4 the final conclusions are drawn.

2. Model

The statistical scission-point model relies on the assumption that the statistical equilibrium is established at scission where the observable characteristics of fission process are formed. The DNS model [12,13,15] is shown to be well suited for describing the scission configuration. The fissioning nucleus at scission point is modeled by two nearly touching coaxial ellipsoids – fragments of the DNS with masses (charges) numbers A_L (Z_L) and A_H (Z_H) for the light (L) and heavy (H) fragments, respectively. Here, $A = A_L + A_H$ ($Z = Z_L + Z_H$) is the mass (charge) number of fissioning nucleus. By taking into consideration the volume conservation, the shape of the system is defined by the mass and charge numbers of the fragments, deformation parameters of fragments, β_i ($i = L, H$), and interfragment distance R. The index i designates the light or heavy fragment of the DNS. The potential energy [15]

$$\begin{aligned} U(A_i, Z_i, \beta_i, R) &= U_L^{LD}(A_L, Z_L, \beta_L) + \delta U_L^{shell}(A_L, Z_L, \beta_L, E_H^*) \\ &+ U_H^{LD}(A_H, Z_H, \beta_H) + \delta U_H^{shell}(A_H, Z_H, \beta_H, E_H^*) \\ &+ V^C(A_i, Z_i, \beta_i, R) + V^N(A_i, Z_i, \beta_i, R) \end{aligned} \quad (1)$$

of the DNS consists of the energies of the fragments and energy $V^C + V^N$ of their interaction. The nuclei in the DNS have the excitation energies E_i^*. The energy of each fragment consists of the excitation-energy-dependent liquid-drop energy U_i^{LD} and deformation-dependent shell-correction term δU_i^{shell} calculated with the Strutinsky method and the two-center shell model [16]. The damping of the shell corrections with excitation energy E_i^* is introduced as

$$\delta U_i^{shell}(A_i, Z_i, \beta_i, E_i^*) = \delta U_i^{shell}(A_i, Z_i, \beta_i, E_i^* = 0) \exp[-E_i^*/E_D], \quad (2)$$

where $E_D = 18.5$ MeV is the damping constant. The interaction potential consists of the Coulomb interaction potential V^C of the two uniformly charged ellipsoids and nuclear interaction potential V^N in the double-folding form [17]. The interaction potential has a potential pocket with external barrier located at the distances between the tips of the fragments of about (0.5–1) fm and (1.5–2) fm [in the considered region of fission fragments], respectively, depending on deformations of the fragments. The internuclear distance R in Eq. (1) corresponds to the position $R = R_m(A_i, Z_i, \beta_i)$ of the minimum of this pocket. The quasifission barrier, $B_{qf}(A_i, Z_i, \beta_i)$, calculated as the difference of the potential energies at the bottom of the potential pocket [$R = R_m(A_i, Z_i, \beta_i)$] and at the top of the external barrier [$R = R_b(A_i, Z_i, \beta_i)$], prevents the decay of the DNS in R [18]. Note that the height of the quasifission barrier decreases with charge asymmetry.

Because the thermal equilibrium is assumed at scission point, the excitation energy $E^*(A_i, Z_i, \beta_i, R_m)$ at scission is calculated as the initial excitation energy of fissioning nucleus $E_{CN}^* = E_n + Q$ (E_n is the neutron kinetic energy) plus the difference between the potential energies of fissioning nucleus $U_{CN}(A, Z, \beta)$ and of the system at the scission point $U(A_i, Z_i, \beta_i, R_m)$ [12,15]: $E^*(A_i, Z_i, \beta_i, R_m) = E_{CN}^* + [U_{CN}(A, Z, \beta) - U(A_i, Z_i, \beta_i, R_m)]$. The relative formation probability of the DNS with particular masses, charges and deformations of the fragments is statistically calculated as follows [18]:

$$\begin{aligned} &w(A_i, Z_i, \beta_i, E^*) \\ &= N_0 \exp\left[-\frac{U(A_i, Z_i, \beta_i, R_m) + B_{qf}(A_i, Z_i, \beta_i)}{T}\right], \end{aligned} \quad (3)$$

where N_0 is the normalization factor. In Eq. (3), the temperature is calculated as $T = \sqrt{E^*/a}$, where $a = A/12$ MeV^{-1} is the level density parameter in the Fermi-gas model [14]. In our calculations, a single value is used for the temperature at the global potential minimum of U before the shell damping. As seen, the height B_{qf} of the quasifission barrier has also an impact on the yields. With increasing elongation and decreasing charge (mass) asymmetry the value of B_{qf} decreases, the system becomes more unstable and decays.

In order to obtain the mass–charge distribution of fission fragments, one should integrate (3) over β_L and β_H:

$$Y(A_i, Z_i, E^*) = N_0 \int d\beta_L d\beta_H w(A_i, Z_i, \beta_i, E^*). \quad (4)$$

The ratio of the yields of fragments with different charge/mass numbers is mainly governed by the difference in energy between the corresponding potential minima in the plane (β_L, β_H), as seen in Eq. (3). For the two potential energy surfaces with minima, which are close in energy, a higher yield stems from the DNS with a wider and shallower minimum, and lower yield emerges from an abrupt and narrow minimum. This is a direct result of Eq. (4) [15]. For the calculations of mass and charge distributions, the following expressions are used:

$$\begin{aligned} Y(A_i, E^*) &= \frac{\sum_{Z_i} Y(A_i, Z_i, E^*)}{\sum_{Z_i, A_i} Y(A_i, Z_i, E^*)}, \\ Y(Z_i, E^*) &= \frac{\sum_{A_i} Y(A_i, Z_i, E^*)}{\sum_{Z_i, A_i} Y(A_i, Z_i, E^*)}. \end{aligned} \quad (5)$$

Because the dynamical treatment is not explicitly performed here, we simulate the dynamical effects by restricting the minimum value of the quasifission barrier. In the calculations, we take into consideration only those configurations for which B_{qf} is larger than ~ 1 MeV. This condition restricts the highly deformed unstable configurations in the (β_L, β_H) plane and, correspondingly, restricts the upper limits of integration over deformations $\beta_{L,H}$. As shown below, the experimental data are described well with this restriction.

3. Calculated results

The experimental [2] and calculated charge distributions resulted from the electromagnetic ($E_\gamma = 11$ MeV) induced fission of even–even nuclei ^{204,206,208}Rn, ^{210,212,214,216,218}Ra, ^{222,224,226,228}Th, and ^{230,232,234}U are shown in Figs. 1–3. As seen, our model is suitable for describing both symmetric and asymmetric charge distributions, and shows good agreement with the experimental data. For the isotopes of Rn [Fig. 1] and Ra [Fig. 2], and ^{222}Th [Fig. 3], the fragment charge distributions are clearly symmetric, with a single prominent peak around $Z/2$, while the charge distributions of fissioning nuclei ^{228}Th [Fig. 3] and ^{230,232,234}U [Fig. 1] have two distinct asymmetric peaks. The fission of the ^{226}Th nucleus ($N = 136$) shows a three-peaked distribution [Fig. 3]. The evolution of the shape of charge distribution with increasing neutron number of fissioning nucleus Ra also displays similar features [Fig. 4] as in the case of fissioning nucleus Th. The symmetric fission of ^{220}Ra is evident. The formation of the asymmetric peaks starts at $A = 222$, while at $A = 224$ ($N = 136$) three-equal-peaks are formed. The fission of ^{226}Ra generates an asymmetric distribution. A small symmetric contribution still exists, although not so

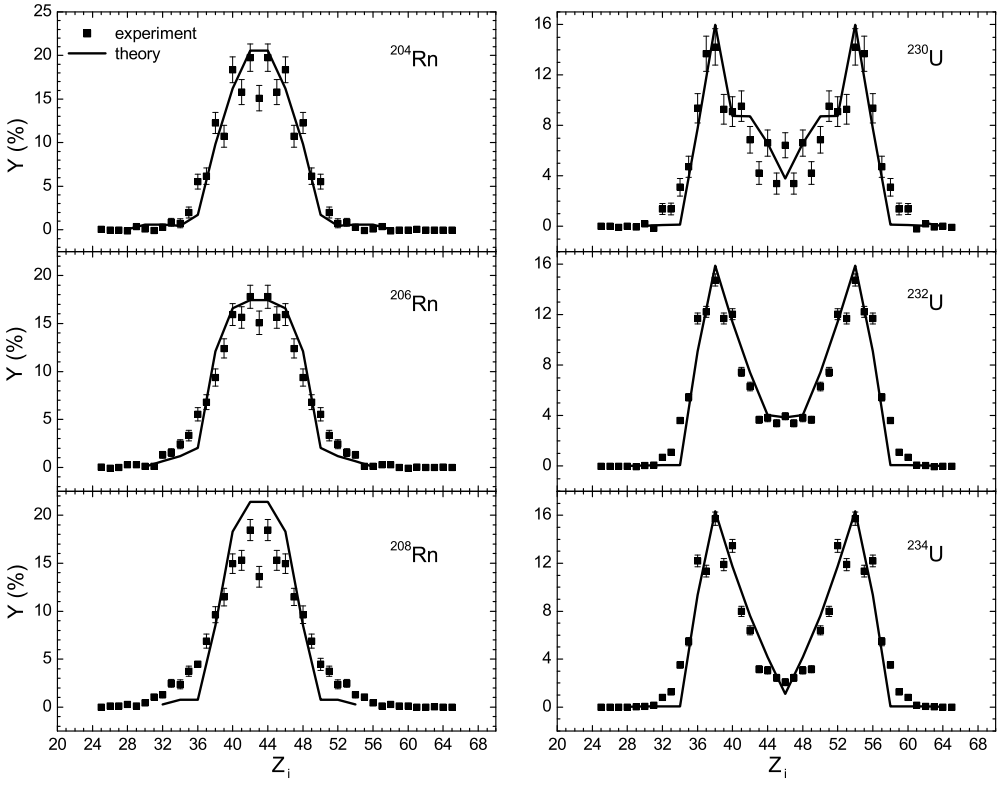

Fig. 1. The calculated charge distributions (lines) for electro-magnetic-induced fission of the indicated radon and uranium isotopes at 11 MeV excitation energy are compared with the experimental data [2] (symbols). The lines connect the calculated points for even–even fission fragments.

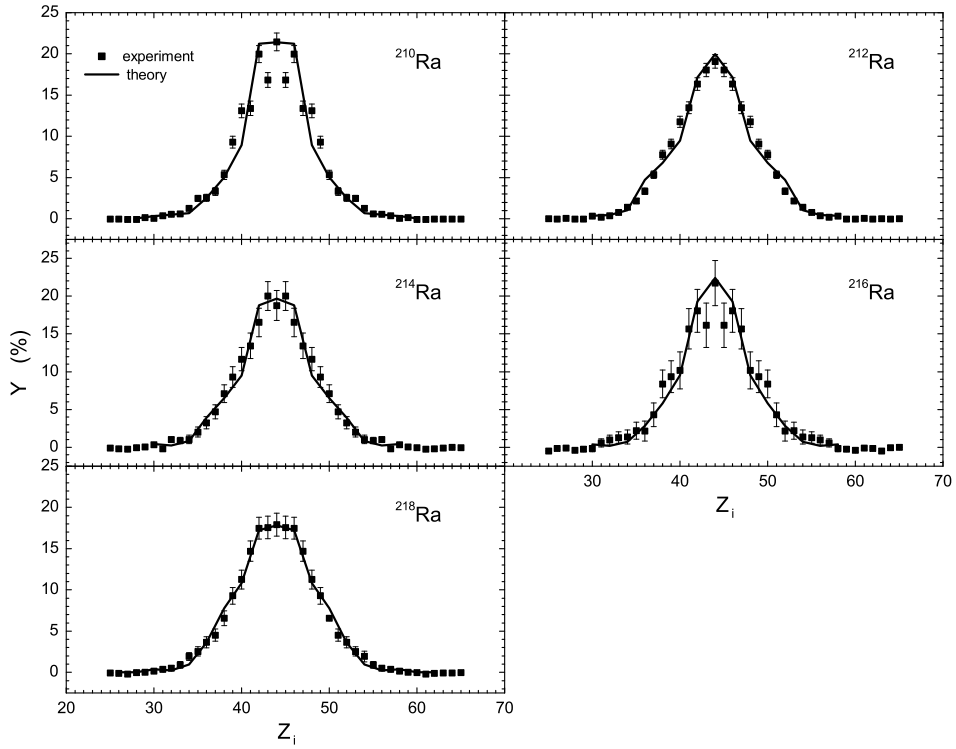

Fig. 2. The same as in Fig. 1, but for the indicated radium isotopes.

evident as in the fission of ^{228}Th. In Fig. 5, the charge yields are predicted for the fission of $^{222}Rn_{136}$ and $^{228}U_{136}$ at 11 MeV excitation energy. In both cases, the three-peaked charge distribution is obtained at low excitation energy.

The transition from one-peaked to two-peaked distribution, going through the transient three-peaked shape, can be explained by studying the driving potential $U(Z_i) = U(A_i, Z_i, \beta_i, R_m)$ of the system [Eq. (1)]. Here, the values A_i and β_i are related to Z_i to supply

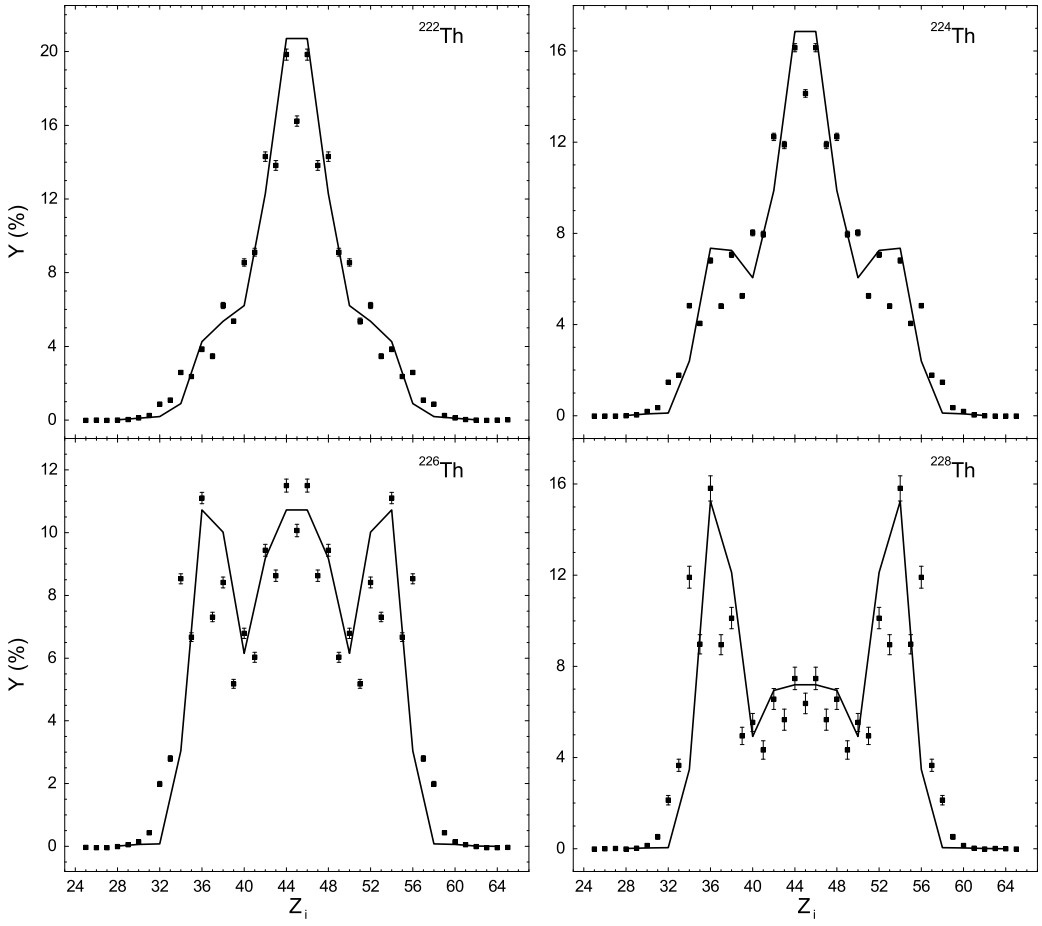

Fig. 3. The same as in Fig. 1, but for the indicated thorium isotopes.

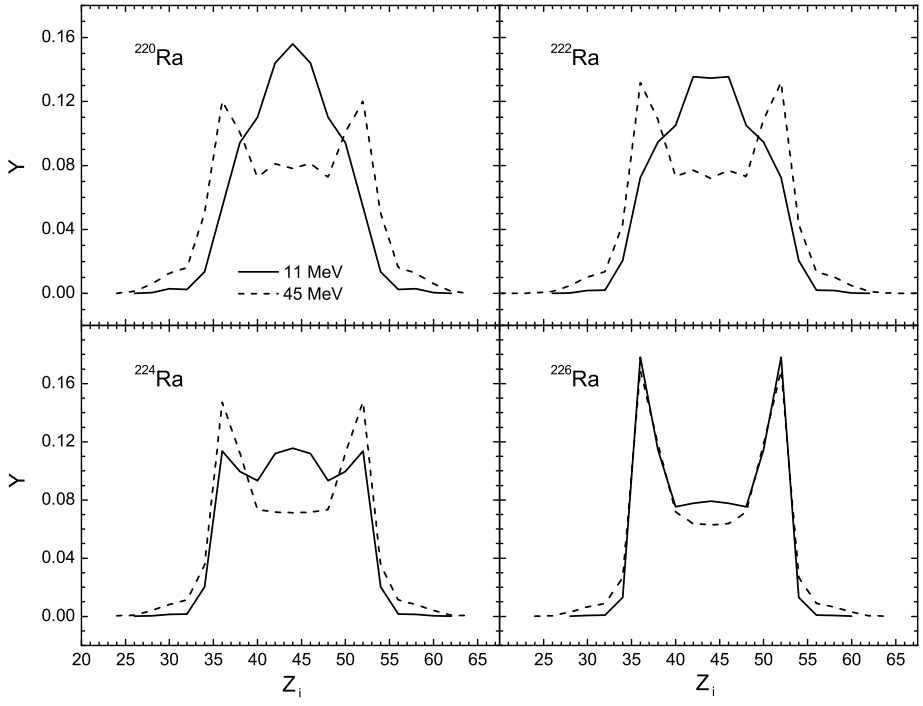

Fig. 4. The predicted charge distributions for the fission of ^{220,222,224,226}Ra at 11 MeV (solid line) and 45 MeV (dashed line) excitation energies of the initial compound nuclei. The lines connect the calculated points for even–even fission fragments.

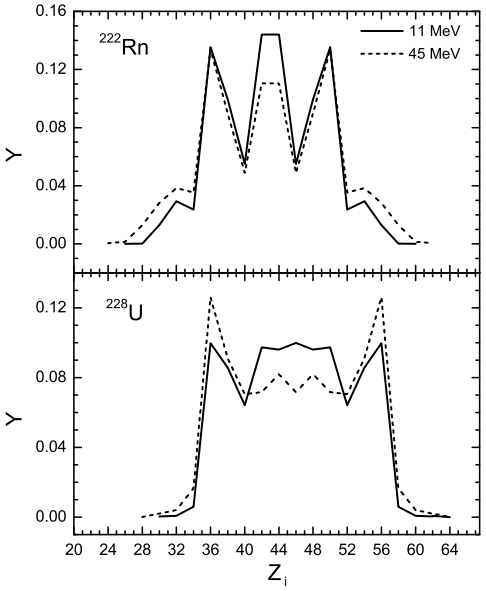

Fig. 5. The same as in Fig. 4, but for the nuclei ^{222}Rn and ^{228}U.

Table 1
The calculated equilibrium deformations of the dinuclear system nuclei and potential energy $U(Z_i)$ are presented for the various fragmentations of the fissioning nucleus ^{224}Ra at 11 MeV excitation energy. The driving potential is normalized to the energy $U(Z/2) = 0$ MeV. The deformation β_i $(i = L, H)$ is given as the ratio between the major and minor semi-axis of the nucleus "i".

Fragmentation	β_L	β_H	$U(Z_i)$ (MeV)
^{60}Cr + ^{164}Gd	1.45	1.45	8.39
^{64}Fe + ^{160}Sm	1.6	1.5	7.17
^{66}Fe + ^{158}Sm	1.65	1.5	6.98
^{70}Ni + ^{154}Nd	1.65	1.45	5.62
^{74}Zn + ^{150}Ce	1.8	1.4	5.59
^{76}Zn + ^{148}Ce	1.3	1.55	5.25
^{82}Ge + ^{142}Ba	1.4	1.3	5.04
^{84}Se + ^{140}Xe	1.4	2.0	2.91
^{86}Se + ^{138}Xe	1.3	1.95	2.3
^{88}Kr + ^{136}Te	1.45	1.95	2.14
^{90}Kr + ^{134}Te	1.55	1.2	1.7
^{92}Kr + ^{132}Te	1.6	1.25	1.26
^{94}Kr + ^{130}Te	1.65	1.25	2.90
^{94}Sr + ^{130}Sn	1.6	1.2	2.02
^{96}Sr + ^{128}Sn	1.65	1.25	1.32
^{98}Sr + ^{126}Sn	1.6	1.4	1.76
^{100}Zr + ^{124}Cd	1.6	1.7	1.82
^{102}Zr + ^{122}Cd	1.75	1.5	1.41
^{104}Zr + ^{120}Cd	1.2	1.85	2.33
^{104}Mo + ^{120}Pd	1.7	1.55	2
^{106}Mo + ^{118}Pd	1.7	1.55	0.25
^{108}Mo + ^{116}Pd	1.65	1.55	0.83
^{108}Ru + ^{116}Ru	1.7	1.55	2.95
^{110}Ru + ^{114}Ru	1.7	1.55	0.59
^{112}Ru + ^{112}Ru	1.65	1.65	0

the minimum of U. For the nuclei ^{220,222,224,226}Ra, we present the ratio between the potential energy $U_{Z_i} = U(A_i, Z_i, \beta_i, R_m)$ and the nuclear temperature T [Fig. 6]. For ^{220}Ra, the driving potential shows a deep and relatively narrow minimum at $Z/2 = 44$ [Fig. 6]. For ^{222}Ra, $U(Z_i)$ starts displaying the formation of the second minimum around the configurations with Se and Kr which becomes well developed at $A = 224$. Even though the second minimum is higher by ~ 1 MeV than $U(Z/2)$, the corresponding yields are the same. This is easily explained by the facts that in (β_L, β_H) surface, the potential minima for the configurations with Se and Kr are wider than those for the configurations Ru + Ru, and there are several mass fragmentations with the $Z_L = 34$ and 36 and potential energies about 1 MeV which contribute to the charge yields. The driving potential for ^{226}Ra exhibits three equal minima. However, the asymmetric mode dominates because of the same reasons as in the case of ^{224}Ra.

One can explain the three-peaked fission-fragment charge distributions resulting from the fission of nuclei with $N = 136$ by examining the driving potential (see Table 1). The fragmentations with $Z_L = 34$ and 36 spawn fragments with the magic neutron number either $N_L = 50$, as in the cases of ^{84}Se + ^{140}Xe and ^{86}Kr + ^{138}Te, or complementary fragments with $N_H = 82$, such as ^{88}Se + ^{136}Xe and ^{90}Kr + ^{134}Te. The configurations Sr + Sn contain the fragments with the closed proton shell $Z_H = 50$ and the neutron number N_H in the vicinity of the magic number 82. The fragmentations with Zr also come with complementary fragments close to $N_H = 82$ (for example, ^{100}Zr + ^{124}Cd). The presence of the closed neutron and proton shells favors the configurations with $Z_L = 34, 36,$ and 38, and, even though their $U(Z_i)$ are higher by 1 MeV than for the symmetric division, the large number of mass fragmentations and the large width of the potential minima in the deformation plane (β_L, β_H) promote large yields in this charge region. The strong shell effects are also expressed in relatively small deformations of the corresponding nuclei, as seen in Table 1.

For the nuclei with mass numbers larger than $A_L = 104$ the shell effects are almost negligible, as Z_L (N_L) are midway between proton (neutron) numbers of the closed shells. This leads to an almost pure liquid drop behavior of the system that causes higher deformations of the fragments (Table 1). So, the higher deformations lead to smaller interaction energy and total potential energy, and more symmetric fragmentations are favorable. The liquid-drop behavior of the system is also reflected in the quick increase of the driving potential when the charge (mass) number deviates from $Z/2$ $(A/2)$. This is the physics origin of the central peak in the charge distribution.

Whenever the neutron number $N = 136$ appears, the fission fragments are expected to display a three-peaked charge distribution due to the large number of configurations with $N_L = 50$, $N_H = 82$, and $Z_H = 50$, or proton/neutron numbers close to these magic numbers. The large number of potential energy surfaces (β_L, β_H) with similar U reiterates the importance of the multidimensional aspect of the potential energy. A central peak is also expected to appear, as it has origin in the liquid-drop nature of the fissioning nuclei because the symmetric fragments have the mid-closed shells.

The predicted mass distributions for the fission of nuclei ^{220,222,224,226}Ra at 11 MeV excitation energy are shown in Fig. 7. At $A = 222$ and 224 the mass distributions display a single narrow peak around $Z/2$, while for the ^{226}Ra nucleus there is a plateau in the mass range $A_L = 92$–104 alongside a sharp narrow peak around mass numbers 106–118 which is higher by about 40% than the plateau. For the ^{226}Ra nucleus, there is the three-peaked mass distribution with a central peak smaller than the asymmetric ones.

In Figs. 4, 5, and 7, we also show the charge and mass distributions of the fissioning nuclei ^{222}Rn, ^{220,222,224,226}Ra, and ^{228}U at the excitation energy of 45 MeV. In all cases the asymmetric component is strongly enhanced. This is explained on the basis that with increasing excitation energies previously inaccessible asymmetric configurations are involved. For the fissioning nucleus ^{226}Ra, the symmetric component is completely suppressed. For the fissioning nuclei ^{222}Rn and ^{228}U [Fig. 5] the charge yields show similar behavior as in the case of the ^{224}Ra nucleus. Note that the change of the charge distribution with excitation energy is rather weak in the case of ^{222}Rn.

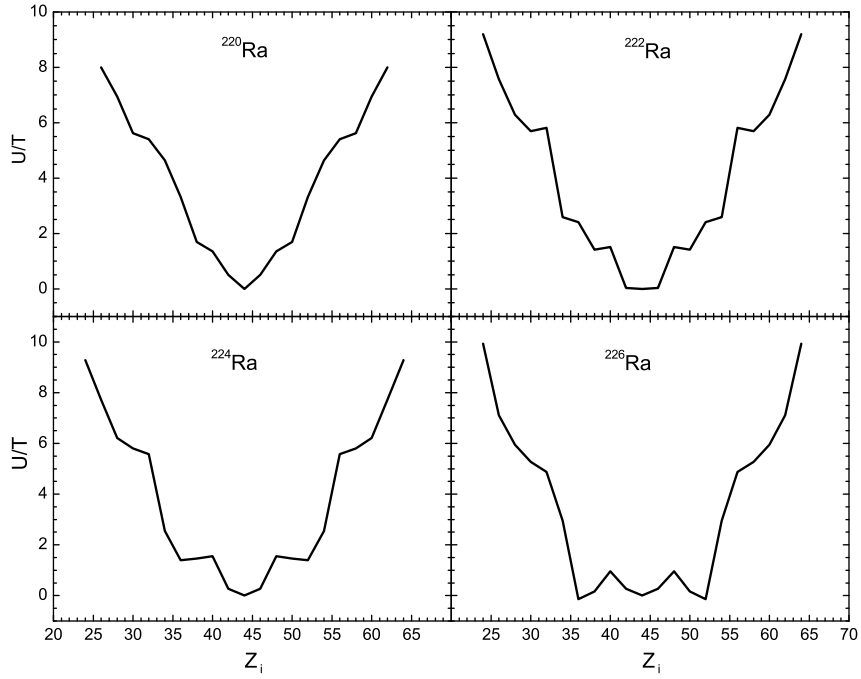

Fig. 6. The calculated ratios $U(Z_i)/T$ between the potential energy and nuclear temperature for the fission of indicated radium isotopes at 11 MeV excitation energy. The potentials are normalized to the energy $U(Z/2) = 0$ MeV. The values of A_i and β_i are related to Z_i to supply the minimum of U.

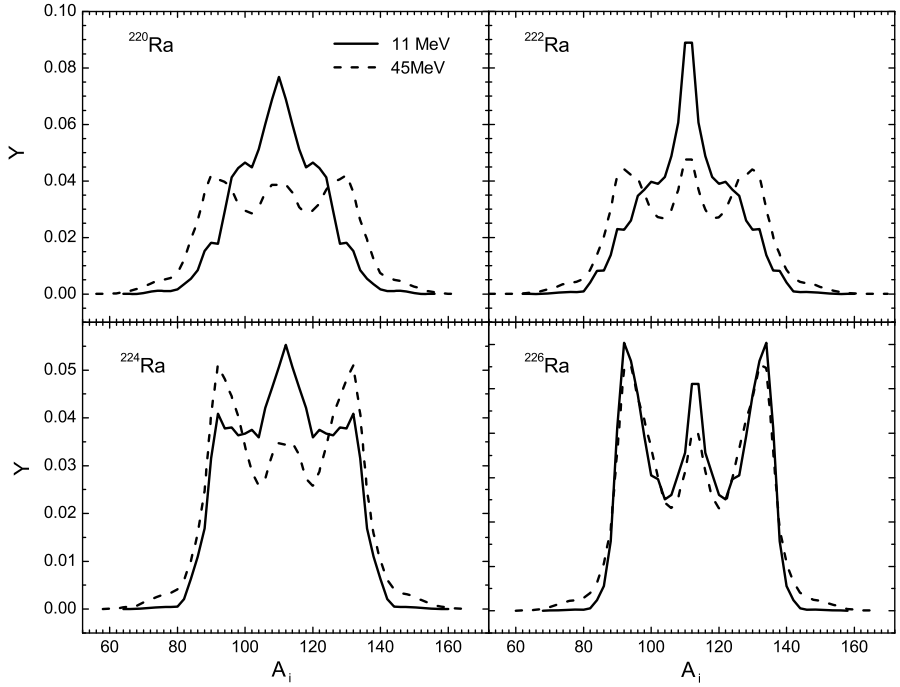

Fig. 7. The predicted mass distributions for the fission of ^{220,222,224,226}Ra at 11 MeV (solid line) and 45 MeV (dashed line) excitation energies of the initial compound nuclei. The lines connect the calculated points for even–even fission fragments.

4. Conclusions

The improved scission-point model provides a good agreement with the experimental charge distributions of the fissioning nuclei ^{204,206,208}Rn, ^{210,212,214,216,218}Ra, ^{222,224,226,228}Th, and ^{230,232,234}U. With increasing neutron number of fissioning nucleus the transition from symmetric to asymmetric fission mode is shown to be related to the change of the potential energy surface at the scission point. The evolution from a one-, to three- and then two-peaked distribution is expected to occur across several mass units. The three-equal-peaked charge distributions are predicted for the fissioning nuclei ^{222}Rn, ^{224}Ra, and ^{228}U with the neutron number $N = 136$. Our model predicts the presence of symmetric and asymmetric fission modes with equal probabilities at $N = 136$, regardless of the charge number of the fissioning system. The explanation relies on the large number of configurations with $N_L = 50$, $N_H = 82$, $Z_H = 50$ or with proton/neutron numbers close to these magic numbers, the large width of the potential

minima in the deformation space (β_L, β_H), and the liquid-drop behavior of the symmetric configurations. Our calculations also demonstrate that the asymmetric component remain to be favored at high excitation energies for systems with $N \sim 136$. For the experimental verification of our predictions, one can suggest to study the following transfer-induced fission reactions: ^{48}Ca + ^{226}Ra $\rightarrow$ ^{222}Rn (fission) + ^{52}Ti, ^{48}Ca + ^{208}Pb $\rightarrow$ ^{222}Rn (fission) + ^{34}S, ^{40,48}Ca + ^{226}Ra $\rightarrow$ ^{224}Ra (fission) + ^{42,50}Ca, and ^{40}Ca + ^{238}U $\rightarrow$ ^{228}U (fission) + ^{50}Ca at incident energies near the corresponding Coulomb barriers.

Acknowledgements

G.G.A. and N.V.A. acknowledge the partial supports from the Alexander von Humboldt-Stiftung (Bonn), DFG (Bonn), and the Russian Foundation for Basic Research (Moscow). The Romania-JINR (Dubna) Cooperation Programme is gratefully acknowledged.

References

[1] A.N. Andreyev, M. Huyse, P. Van Duppen, Rev. Mod. Phys. 85 (2013) 1541.
[2] K.-H. Schmidt, et al., Nucl. Phys. A 665 (2000) 221;
K.-H. Schmidt, et al., Nucl. Phys. A 693 (2001) 169.
[3] M.G. Itkis, N.A. Kondratíev, S.I. Mulígin, V.N. Okolovich, A.Ya. Rusanov, G.N. Smirenkin, Sov. J. Nucl. Phys. 53 (1991) 757.
[4] I.V. Ryzhov, et al., Phys. Rev. C 83 (2011) 054603.
[5] U. Brosa, S. Grossmann, A. Müller, Phys. Rep. 197 (1990) 167.
[6] J. Randrup, P. Möller, Phys. Rev. Lett. 106 (2011) 132503;
J. Randrup, P. Möller, Phys. Rev. C 84 (2011) 034613;
P. Möller, J. Randrup, A.J. Sierk, Phys. Rev. C 85 (2012) 024306.
[7] B.D. Wilkins, E.P. Steinberg, R.R. Chasman, Phys. Rev. C 14 (1976) 1832.
[8] T. Matsuse, C. Beck, R. Nouicer, D. Mahboub, Phys. Rev. C 55 (1997) 1380.
[9] S.J. Sanders, A. Szanto de Toledo, C. Beck, Phys. Rep. 311 (1999) 487.
[10] S. Panebianco, J.-L. Sida, H. Goutte, J.-F. Lemaître, N. Dubray, S. Hilaire, Phys. Rev. C 86 (2012) 064601.
[11] M. Caamaño, et al., Phys. Rev. C 92 (2015) 034606.
[12] A.V. Andreev, G.G. Adamian, N.V. Antonenko, S.P. Ivanova, W. Scheid, Eur. Phys. J. A 22 (2004) 51;
A.V. Andreev, G.G. Adamian, N.V. Antonenko, S.P. Ivanova, Eur. Phys. J. A 26 (2005) 327.
[13] A.V. Andreev, G.G. Adamian, N.V. Antonenko, Phys. Rev. C 86 (2012) 044315;
A.V. Andreev, G.G. Adamian, N.V. Antonenko, A.N. Andreyev, Phys. Rev. C 88 (2013) 047604.
[14] G.G. Adamian, N.V. Antonenko, W. Scheid, in: C. Beck (Ed.), Clusters in Nuclei, vol. 2, in: Lect. Notes Phys., vol. 848, Springer-Verlag, Berlin, 2012, p. 165.
[15] H. Pașca, G.G. Adamian, N.V. Antonenko, A.V. Andreev, Y. Kim, Phys. Rev. C 93 (2016) 054602;
H. Pașca, EPJ Web Conf. 107 (2016) 07003, http://dx.doi.org/10.1051/epjconf/201610707003.
[16] J. Maruhn, W. Greiner, Z. Phys. 251 (1972) 431.
[17] G.G. Adamian, et al., Int. J. Mod. Phys. E 5 (1996) 191.
[18] Sh.A. Kalandarov, G.G. Adamian, N.V. Antonenko, W. Scheid, Phys. Rev. C 82 (2010) 044603;
Sh.A. Kalandarov, G.G. Adamian, N.V. Antonenko, W. Scheid, Phys. Rev. C 83 (2011) 054611;
Sh.A. Kalandarov, G.G. Adamian, N.V. Antonenko, W. Scheid, J.P. Wieleczko, Phys. Rev. C 84 (2011) 064601.